RSC Advances

PAPER

View Article Online
View Journal | View Issue

Cite this: *RSC Adv.*, 2024, **14**, 29763

Cu-doped ZnO/Ag/CuO heterostructure: superior photocatalysis and charge transfer†

Abbay Gebretsadik,[a] Bontu Kefale,[a] Chaluma Sori,[a] Dereje Tsegaye,[a] H. C. Ananda Murthy ‡*[b] and Buzuayehu Abebe *[a]

Doped semiconductor heterostructures have superior properties compared to their components. In this study, we observed the synthesis of Cu-doped ZnO/Ag/CuO heterostructure with the presence of charge transfer and visible light-harvesting properties resulting from doping and heterojunction. The porous heterostructures were prepared using the bottom-up combustion (BUC) approach. This method generated porous heterostructures by eliminating gaseous by-products. X-ray diffraction (XRD) optimization revealed that the ideal conditions included 1.00 g of polyvinyl alcohol (PVA), a synthesis temperature of 50 °C, and a 1 hour calcination time. Introducing copper (Cu) into the zinc oxide (ZnO) lattice caused a high-angle shift in the XRD pattern peaks. High-resolution transmission electron microscopy (HRTEM) images and XRD patterns confirmed the formation of Cu-doped ZnO/Ag/CuO (c-zac) heterostructures. Elemental mapping analysis confirmed the even surface distribution of Ag metal. The c-zac heterostructures exhibited superior optoelectrical and charge transfer properties compared to single ZnO. The heterostructures demonstrated improved methylene blue (MB) dye degradation potential ($k = 0.065\ min^{-1}$) compared to single ZnO ($k = 0.0041\ min^{-1}$). This photocatalytic potential is attributed to enhanced light absorption and charge transfer properties. The extended visible light absorption resulted from CuO and Ag's surface plasmon resonance properties. The selected 15c-zac heterostructure also performed well in a reusability photocatalytic test, remaining effective until the 3rd cycle. Consequently, this heterostructure holds promise for scaling up as a catalyst for environmental remediation.

Received 18th August 2024
Accepted 13th September 2024

DOI: 10.1039/d4ra05989a

rsc.li/rsc-advances

1. Introduction

A large volume of non-biodegradable pollutants that induce toxicity in human and aquatic systems are discharged into water bodies without treatment.[1] Therefore, researchers should develop efficient organic pollutants remediation techniques using nanotechnology. Metal oxides such as zinc oxide (ZnO) and titanium oxide (TiO_2) have decent optoelectronic properties, environmental friendliness, stability, and photocatalytic activities.[2] However, light-induced electron–hole recombination and a lack of harvesting visible light are the main ZnO drawbacks. Porous metal or metal oxide heterostructures and doping strategies are the two novel approaches to improving host material drawbacks.[3–5] Besides, material with visible light absorption properties, which constitute about 40% of the solar spectrum, has valuable use in several applications.[2,6]

Copper ion (Cu^{2+}) has comparable ionic radii with zinc ion (Zn^{2+}). The ionic radius of Cu^{2+} is 0.58 Å in tetrahedral and 0.73 Å in octahedral coordination, while the ionic radius of Zn^{2+} is 0.60 Å in tetrahedral and 0.74 Å in octahedral coordination. Thus, the penetration and inclusion of these slightly smaller ionic radii of Cu^{2+} result in lattice shrinkage, which results in a peak shift towards a high angle on the XRD pattern.[7] Copper doping forms 3d mid-gap state in the ZnO band gap and acts as an electron trap and interband transition.[8] Besides, the greater ionic radii of silver compared to the zinc ion increase the ZnO's unit cell volume and result in the shifting of the XRD pattern peak towards a lower angle. However, the solubility of silver in the ZnO lattice is difficult due to its greater ionic radii.[9] Thus, it instead forms a separate crystal, or aggregate, as a heterojunction. Trang *et al.*[10] reported a small amount of Ag inclusion in the ZnO lattice based on the XRD pattern peak shift and the domination of heterojunction (independent crystal formation). The Ag crystal then forms local contact with ZnO, which facilitates an *in situ* charge transfer process through the interface. Wang *et al.*[11] also reported the dominance of independent Ag crystal formation instead of its inclusion in the host lattice.

[a]*Department of Applied Chemistry, Adama Science and Technology University, 1888, Adama, Ethiopia. E-mail: buzea8@gmail.com; anandkps350@gmail.com*

[b]*School of Applied Sciences, Papua New Guinea University of Technology, Lae, Morobe Province, 411, Papua New Guinea*

† Electronic supplementary information (ESI) available. See DOI: https://doi.org/10.1039/d4ra05989a

‡ Department of Prosthodontics, Saveetha Dental College & Hospital, Saveetha Institute of Medical and Technical Science (SIMATS), Saveetha University, Chennai 600077, Tamil Nadu, India.

Recently, the type II (staggered), Z-scheme, and S-scheme charge transfer mechanisms have been proposed. These charge transfer mechanisms are beneficial for boosting the photocatalytic activity of the heterostructure. In the type-II mechanism, charge transfer, Fermi level equilibration, and band-bending processes occur as usual. Under light irradiation, the electrons and holes are separated. Then, the electrons migrate from the more negative conduction band (CB) potential of one semiconductor to the other's less negative CB potential. The holes also migrate from a more positive valence band (VB) potential to a less positive one. With this migration, the electrons have been collected at a position of weaker reducing redox potential. Which means a weaker reduction potential than the standard $O_2/^{\bullet}O_2^-$ reduction potential (−3.33 eV) and weaker oxidation potential than the standard oxidation potential of $^{\bullet}OH/H_2O$ (−2.38 eV). This indicates no full guarantee for water and oxygen to be oxidized and reduced, respectively.[12] In addition, in the traditional Z- and S-scheme mechanisms, the CB electrons and VB holes have greater reduction and oxidation potential, respectively, unlike those in the type II mechanism. However, the CB electrons and VB holes present in the weak reduction and oxidation redox potentials are lost as a result of recombination and quenching. For this reason, recently, the use of noble metals such as silver as charge mediators has been practiced. Besides, the mediator noble metals extend visible light absorption as a result of surface plasmon resonance properties.[13,14] Mahyoub *et al.*[14] synthesised a Z-scheme-based CeO_2/Ag/ZnO heterostructure. As proposed, the electrons migrate from ZnO CB and recombine with VB holes in CeO_2. However, the electrons in the CB of CeO_2 react with oxygen, and holes in the VB of ZnO oxidize water with adequate energy. Silver acts as a mediator and absorbs visible light that constitutes about 40% of the solar spectrum. This visible light absorption for silver is associated with the oscillation of electrons with the electric field.[15]

Recently, several studies have been released for single Ag- and Cu-doped ZnO heterostructure materials. Besides, some works were also reported for Ag and Cu co-doped ZnO heterostructures using different methods, such as chemical bath deposition,[16] sol–gel,[17] facile and low-temperature chemical and photochemical deposition,[18] and co-precipitation.[19] Most of the above-mentioned research works reported the host material property improvement due to copper oxide and silver metal incorporation/heterojunction. However, none of these studies reported synthesizing heterostructures with porous morphology using the bottom-up combustion (BUC) method. The BUC approach follows the development of colloidal NPs in solution, gelation of the colloidal NPs through dehydration, and combustion by heating the dehydrated product to a complex ignition temperature.[20,21] Once the combustion started in many places on the sample surface, a foam-type porous heterostructure was produced. The combustion techniques quickly produce a porous, pure, and highly stable by-product. It needs cheap synthesis equipment and avoids post-synthesis treatment processes.[22] Porosity generation is associated with the evaporation of gaseous by-products. The evolution of gaseous products may further reduce metal ions or metal oxides into zero-valent metal NPs.[23,24] There is also a lack of clarity in proposing the most possible charge transfer and visible light absorption mechanisms. Besides, none of these studies also interconnected the crucial ideas of LaMer's nanocrystal heterostructure growth and the hard soft acid–base (HSAB) dopant–host reactivity balance theory. Optimizing crucial parameters such as synthesis temperature, calcination time, and dopant amount was not also seen in detail.[25–27] During synthesis, optimizing the solution temperature can also assist in controlling the precursor decomposition to nanocrystal growth process, according to LaMer's theory.[28]

Thus, this study synthesized pure NPs and heterostructures using the simple BUC approach. The single NPs and Cu–ZnO/CuO (c-zc), Ag/ZnO (za), and Cu–ZnO/Ag/CuO (c-zac) heterostructures were synthesized in the presence of poly(vinyl alcohol) (PVA) as a capping agent. The effects of PVA amount, synthesis temperature, calcination time, and dopant amount were studied and optimized. The 1.00 g of PVA, 50 °C synthesis temperature, and 1 hour calcination time were obtained to be the optima. The crystallinity and formation of the Cu-doped ZnO/Ag/CuO heterostructure were verified by TEM/HRTEM morphology and XRD pattern analysis. The improved optoelectrical properties of the c-zac were verified from the Mott–Schottky, UV-vis-DRS, and PL analyses. The optimized 15c-zac (15% dopant) heterostructure also showed enhanced methylene blue dye (MB-D) degradation potential with a rate constant value of k 0.067 min^{-1}. This application improvement for c-zac is a result of copper doping and the synergistic effect of CuO, Ag, and ZnO heterostructures.

2. Results and discussion

2.1. Characterization

2.1.1. DTA-TGA investigation. To obtain a catalytically active, stable, and pure final product, the polyvinyl alcohol (PVA) stabilizing agent that was used during synthesis should be removed. This can be done by calcinating the sample at the differential thermal-thermogravimetric analysis (DTA-TGA) optimized temperature in the furnace. The DTA-TGA analysis was used to select the optimal PVA decomposition temperature (Fig. 1). The first small peaks on the DTA plot that appeared lower than 140 °C are associated with surface and crystal-adsorbed dehydration of water. The other wide exothermic DTA band detected within the 150–210 °C temperature range is associated with the decomposition of the complex formed between the nitrate of the zinc precursor and PVA.[29] Lastly, an intense exothermic DTA band was detected within the 300–500 °C temperature range. This intense peak is associated with the pre-formed polyene decomposition. The instability detected beyond 540 °C is due to the thermal oxidation of carbonized residue.[30,31]

Thus, 450 °C is the temperature at which the PVA polymer completely decomposes and gives pure ZnO NPs (as observed from the TGA curve). This temperature of 450 °C was used for further physical analysis (characterization) and application tests.

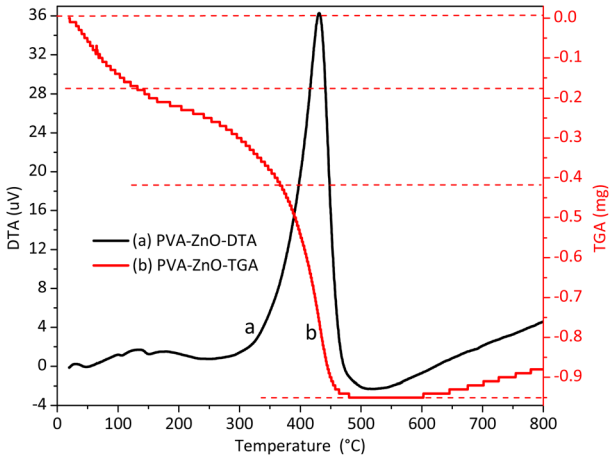

Fig. 1 Thermal analysis: DTA-TGA (differential thermal-thermogravimetric analysis) plots of polyvinyl alcohol–zinc precursor complexes before calcinating the sample in the furnace.

2.1.2. XRD investigation. The XRD pattern of PVA, NPs, and heterostructures synthesized using the simple BUC approach is given in Fig. 2 and S1.† The ZnO NPs synthesized without PVA show greater crystallinity and crystallite size (61 nm) than ZnO synthesized using PVA. The smaller crystallite size for ZnO synthesized using PVA indicates that the PVA polymer is acting as a capping agent, which protects the NPs from aggregation. The amount of PVA was also optimized by varying its amount up to 2.00 g (from 0.10 g). Here, 1.00 g of PVA was obtained to be the optimum value (18 nm) (Fig. S1a†). The synthesis solution temperature optimization experiment was conducted by taking different temperatures ranging from 30 °C to 90 °C (Fig. S1b†). In this optimization, the temperature of 50 °C gives a smaller crystallite size. Besides, increasing the calcination time from 30 to 180 min at a fixed temperature of 450 °C resulted in increasing the crystallite size (Fig. S1c†). This indicates that as time increases, the temperature assists in the coalescence process of the NPs. The dopant percentage optimization shows Ag peak starting from lower dopant percentages of 1% (Fig. S1d†). However, the small intensity of CuO-independent peaks was detected only at higher concentrations of 15% and 20%. This indicates that the solubility of copper is better (>5%) than that of silver. The smaller crystallite size of 13 nm was obtained to be the optimum at 15% dopant concentration, which is probably due to the synergistic surface area of copper and silver.

The crystallite size *versus* PVA amount, synthesis temperature, calcination time, and dopant percentage plots were depicted as insets in Fig. S1a–d,† respectively.

Fig. 2 shows the XRD plots of raw PVA, ZnO, Ag, and CuO NPs, and c-zac heterostructure (15%). The PVA XRD pattern has a peak at 20°, which corresponds to the crystal plane of (101) (JCPDS # 00-053-1847) (see Fig. S1a† inset label a).[32] However, after calcinating the NPs and heterostructures containing PVA polymer at 450 °C, the PVA polymer peaks disappeared, indicating the complete decomposition of it. The 2θ values with the respective crystal planes of single ZnO NPs are 31.8 (100), 34

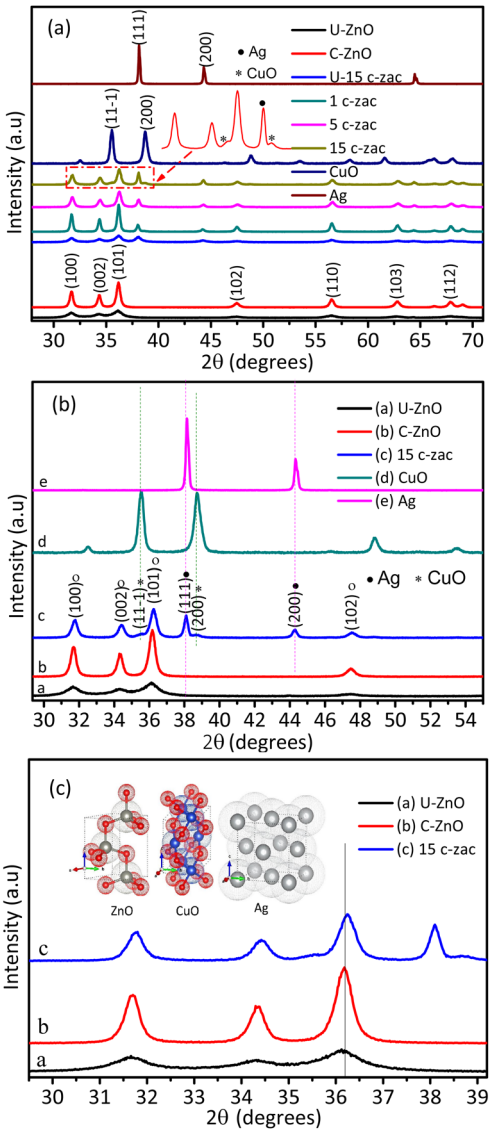

Fig. 2 XRD crystallite structure of NPs and c-zac heterostructure: (a) the X-ray diffraction patterns of ZnO nanoparticles, and c-zac heterostructures, (b and c) the magnified views of uncalcined and calcined ZnO and calcined c-zac heterostructures. A copper oxide-independent peak was detected above the 15% dopant amount. The high-angle shift is associated with the dominant copper doping.

(002), 36 (101), 47.5 (102), 56.6 (110), 62.8 (103), and 67.8° (112), revealing the hexagonal wurtzite structure of ZnO NPs (JCPDS # 00-036-1451) (Fig. 2b). The XRD pattern of the c-zac heterostructure also has similar 2θ peaks like that in ZnO and an additional three silver and two small copper oxide (CuO) independent peaks. These three Ag NPs peaks are associated with the fcc structure, which fits with the single Ag 2θ and corresponding crystal planes of 38 (111), 44 (200), and 64° (220) (JCPDS # 00-004-0783). These two CuO peaks appeared at 2θ, and the corresponding crystal planes of 35.5 (002, 11−1) and 39° (200, 111) are associated with the monoclinic structure of CuO (JCPDS # 00-048-1548). The Scherrer formula (eqn (1)) has

been used to calculate the crystallite size of the single NPs and heterostructures.

$$D = \frac{K\lambda}{\beta \cos(\theta)} \quad (1)$$

where D is the mean size of the ordered crystallite, λ is the X-ray radiation wavelength (for CuKα = 0.15418 nm), K is a dimensionless constant related to the shape of the materials, β is the line widening at half maximum intensity, and θ is the diffraction or Bragg angle.

The uncalcinated ZnO NPs and 15c-zac (8 nm) heterostructures show a smaller crystallite size compared to their calcined constituents (Fig. 2). However, depending on the pre-photocatalytic test, the 60 minute calcination time was selected and used for further analysis. Besides, calcinating the material to the optimum time assists in the decomposition of impurities, including the PVA polymer. Depending on the reaction conditions and synthesis approach, substitutional and interstitial doping as well as heterojunction may occur due to the doping of metal or metal ions. The substitutional and interstitial doping can cause peak shifts on the XRD pattern depending on the size of ionic radii. The solubility of silver is very low due to its greater ionic radii, which then form a separate independent crystal.[10,11] Besides, the decomposition of nitrates and PVA complex results in producing gaseous by-products such as NO_2, CO_2, and CO, which reduces silver ions.[24] Thus, Ag forms a more dominant heterojunction with ZnO than that of its inclusion in the host lattice. The dominance of Schottky contact for Ag and ZnO is also consistent with recent reports.[33,34] The radius of the copper ion (0.73 Å) is smaller than zinc ion (0.74 Å) in the tetrahedral structure. Thus, inclusion of copper ions in the ZnO host lattice results in a decrease in unit cell volume and a high angle shift on the XRD pattern.[7] The c-zac heterostructure shows a high angle shift compared to the single ZnO (Fig. 2c). This shift indicates the dominance of copper inclusion in the ZnO lattice. The appearance of silver and copper oxide (CuO) peaks on the XRD patterns of 15c-zac indicates the formation of a ZnO/Ag/CuO heterostructure. All together, the formation of Cu-doped ZnO/Ag/CuO heterostructure (c-zac) is witnessed.

2.1.3. DRS-UV-vis, Mott–Schottky, and PL investigation. The optical properties of powder ZnO NPs and c-zac heterostructures were studied by the ultraviolet-visible diffuse reflectance spectroscopy (UV-vis-DRS) technique. The % reflectance *versus* wavelength plot in the DRS-UV-vis spectrum is given in Fig. 3a. The ZnO NPs and heterostructures show sharp reflection at about 390 nm. This reflection is associated with CB electron and VB hole recombination, which is a distinctive property of the ZnO NPs.[35] The direct and indirect bandgaps of the materials can be determined from the Kubelka–Munk (K–M) function by extrapolating the linear region towards the x-axis[36] (Fig. 3b and c). The inter-band electron transition mechanism is dependent on the relative positions of the minimum CB and the maximum VB energy level (which are known as crystal momentum (k-vector) values). The change in minimum CB and maximum VB k-factor for the direct bandgap semiconductor is zero. While the indirect bandgap materials do not have a zero k-factor value.[37] The zero change in k-factor indicates direct emission of the absorbed energy due to electron–hole recombination.

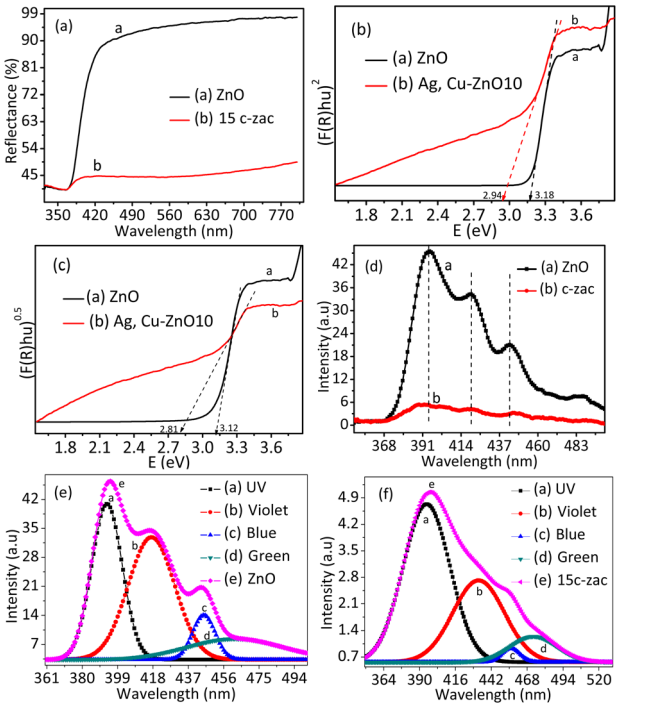

Fig. 3 Optical properties of ZnO NPs and doped heterostructure: (a) the DRS-UV-vis spectra, (b and c) the respective direct and indirect Kubelka–Munk plots of ZnO and c-zac heterostructures, (d) the PL spectra of ZnO and 15c-zac heterostructure, (e and f) the ZnO and c-zac heterostructure Gaussian-shaped constituents of the deconvoluted plots. The inset label 15c-zac denotes the 15% dopant concentration.

However, this electron–hole recombination process diminished in the indirect materials due to the presence of differences in the k-factor values. This indicates that the photon-excited electrons and holes get relaxation time for the reduction and oxidation redox reactions. Thus, the reactive oxygen species obtained from the redox reaction are beneficial for applications such as photocatalysis. The obtained direct and indirect bandgap values of ZnO are 3.18 and 3.12 eV, respectively. The direct and indirect bandgap value for c-zac heterostructure is found to be 2.94 and 2.81, respectively. The c-zac heterostructure showed greater redshift compared to ZnO NPs, indicating the presence of synergistic effects due to copper and silver. Generally, the crystal momentum value for ZnO is zero, indicating it is a direct bandgap material. However, the creation of defects (mid energy level) associated with doping can change the direct transition to an indirect transition, and electrons get relaxation time.[38]

The relative band edge potential and n-type or p-type characters of semiconductor materials can be understood by combining the Mott–Schottky plots and DRS-UV-vis analysis. The Mott–Schottky plots for ZnO NPs and c-zac NCs are depicted in Fig. S2a and b,† respectively. Pure ZnO has positive slopes, indicating it has n-type semiconductivity. The negative

and positive slopes for the 15c-zac heterostructure confirm the p-type and n-type characteristics, respectively. The p-type and n-type characteristics of the 15c-zac heterostructure occur due to the doping and formation of heterojunction and have a close relationship with the improvement of optoelectric properties. From the Mott–Schottky plot, the CB band edge potential can be determined through extrapolation towards the *x*-axis. Thus, the CB band edge potential for ZnO and c-zac is found to be −0.92 V and −0.97 V, respectively, *versus* Ag/AgCl. Supposing that the band edge potential of an n-type semiconductor is 0.1 V more negative,[39] the corrected band edge becomes −0.82 and −0.87 V, respectively. Therefore, we determine the VB edge potential for ZnO and c-zac heterostructure to be 2.12 and 1.94 V, respectively, by combining the Mott–Schottky plots and DRS-UV-vis analysis (VB = E_g + CB).

The optical and luminescence characteristics of ZnO and c-zac heterostructures were also characterised by PL analysis (Fig. 3d). The xenon lamp was used as a source at an excitation wavelength of 325 nm. The common emission band at 394 nm (UV region) is associated with the ZnO-near-band edge emission (NBE) transition as a result of electron–hole recombination. The three emission peaks detected in the visible region are associated with the intrinsic ZnO defects deep-level emission. The visible emission that occurs during synthesis may be associated with electron donor level (V_O and Zn_i) or accepter level (V_{Zn} and O_i) defects. The accepter level occurred below the CB and the donor level above the VB of the host.[40] The violet-blue emission is associated with Zn_i and the host VB transition; the blue emission is associated with V_{Zn} and the host CB transition; green is due to the transition between V_O and V_{Zn}; and yellow is related to the recombination of holes trapped in O_i and electrons in the CB.[41,42]

Fig. 3e and f show the Gaussian-shaped constituents of the deconvoluted plot for ZnO NPs and 15c-zac heterostructure. The intensity of PL spectra used in order to understand the charge recombination efficiently. The lower the PL intensity shows the presence of less charge recombination rate, and the higher the PL intensity, the greater the charge recombination rate.[43] The intensity of UV emission for doped heterostructure decreased from 46 to 5 arbitrary units. This intensity reduction has a direct relationship with electron–hole recombination hindrance or the presence of charge transfer. This enhanced charge transfer is associated with mid-gap level creation due to copper doping as well as heterojunction within the heterostructure interface (ZnO/Ag/CuO).[14,44] This charge transfer process with delayed charge recombination has great importance in different applications, such as catalysis and photocatalysis.[45,46] The UV, violet, blue, and green emission for ZnO NPs was observed at about 394, 418, 446, and 460 nm. However, the respective emission peaks for the c-zac heterostructure were observed at 397, 420, 445, and 466 nm, respectively. The UV and blue emissions for the doped heterostructure showed a redshift compared to the ZnO NPs, which is due to the host dopant sp–d strong exchange interaction.[47,48] This host electron interaction with localized unpaired dopant 3d electrons creates a new mid-gap level between the host bandgap.

2.1.4. Morphological investigation. In the BUC synthesis approach, once the combustion started at the ignition point of the precursor–PVA complex, the evolution of gaseous by-products started. Then, either a long wire- or spongy-like structure occurs depending on whether the evolution started at one or many points.[23,49] The FESEM images of ZnO NPs and c-zac heterostructure for this study show a spongy-like structure, which resulted from the evolution of gases from many points (Fig. 4a and 5a). Besides, the gaseous by-products react with metal ions and result in the reduction of metals.[23] The c-zac heterostructure has a more spongy-like structure compared to ZnO NPs, indicating silver and copper salts are facilitating the combustion process more. The surface distribution of dopant is a crucial concern for several applications.[50,51] Fig. 4b and 5b show EDS elemental mapping analyses for ZnO NPs and c-zac heterostructure, respectively. The elemental mapping analyses for zinc and oxygen are depicted in Fig. 4b2 and b3, respectively. The elemental mapping analyses for zinc, copper, silver, and oxygen are depicted in Fig. 5b1–b4, respectively. The EDS-layered image of c-zac heterostructure shows a good distribution of copper and silver dopants on the host surface. The elemental mapping image of silver shows white dots (Fig. 5b3). These white dots are also visible on the FESEM image with a good distribution, which are the reduced silver metal during gas evolution.

The presence of only expected elements in the EDX elemental composition analysis also shows material purity (Fig. S3a and b†). The obtained composition for copper is lower than the amounts added during synthesis, which is probably its inclusion in the ZnO lattice and its likeness to zinc.

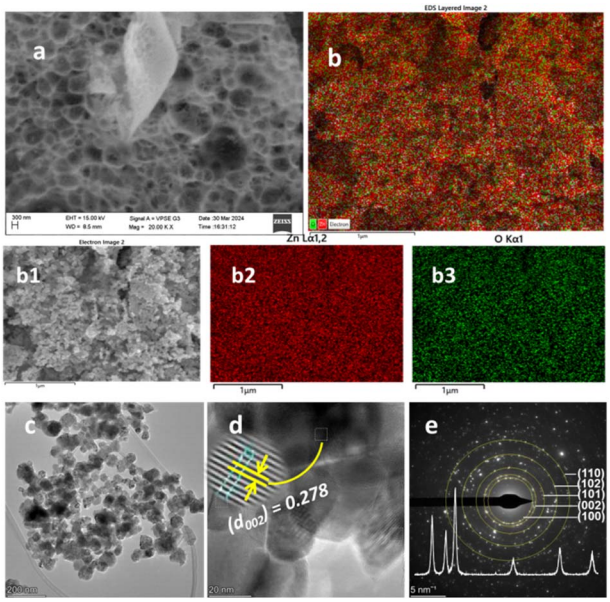

Fig. 4 Morphological and elemental mapping analysis of ZnO NPs: (a) FESEM image, (b) EDS layered image, (b1) electron image, (b2 and b3) elemental mapping images of zinc and oxygen, respectively, (c–e) TEM image, HRTEM, and SAED ring of ZnO NPs, respectively. The inset in (e) is the X-ray diffraction pattern. The scale bar for image (a) is 300 nm, for (b), (b1), (b2), and (b3) is 1 μm, for (c) is 200 nm, for (d) 20 nm, and for (e) 5 nm^{-1}.

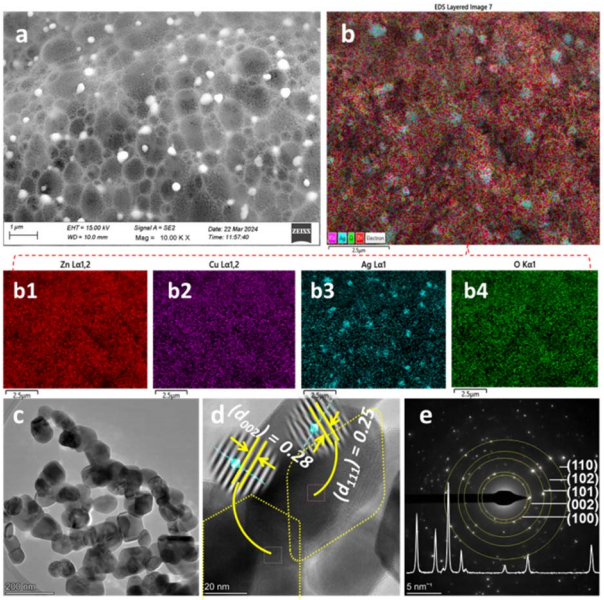

Fig. 5 Morphological and elemental mapping analysis of c-zac heterostructure: (a) FESEM image, (b) EDS layered image, (b1–b4) elemental mapping images of zinc, copper, silver, and oxygen, respectively, (c–e) TEM image, HRTEM, and SAED ring of c-zac heterostructure, respectively. The inset in (e) is the X-ray diffraction pattern. The scale bar for image (a) is 1 μm nm, for (b), (b1), (b2), (b3), and (b4) is 2.5 μm, for (c) is 200 nm, for (d) 20 nm, and for (e) 5 nm^{-1}.

The TEM/HRTEM/SAED images of ZnO and 15c-zac heterostructures are depicted in Fig. 4c–e and 5c–e, respectively. The TEM images of ZnO and 15c-zac heterostructures are depicted in Fig. 4c and 5c, respectively. The image has an agglomerated but less aggregated morphology with a size between 20 and 65 nm. The doped heterostructure also shows more additional porosity and channels compared to bare ZnO NPs. This porosity and channel occur during the evolution of gaseous by-products.[23] Fig. 4d and 5d show the HRTEM image analysis for ZnO NPs and c-zac heterostructure, respectively. The *d*-spacing value of 0.278 nm, obtained from the HRTEM image, for single ZnO NPs matches with the (002) plane of the ZnO crystals. The *d*-spacing values of 0.280 and 0.25 nm on the c-zac heterostructure are associated with ZnO and Ag crystals, respectively. These *d*-spacing values correspond to the hexagonal (022) plane of ZnO and the spherical (111) plane of Ag crystallites. The existence of Ag crystals indicates the presence of local contact (Schottky contact) between ZnO and Ag crystals.[18,33] Fig. 4e and 5e show the SAED ring images for ZnO and c-zac heterostructures, respectively. The ring and white spots in the SAED image show the crystalline nature of the materials.

2.1.5. FTIR investigation. The metal–oxygen bond and functional group information can be understood from the FT-IR spectroscopic technique. The FTIR analysis was conducted for calcined and uncalcined materials (Fig. S4a†). As usual, the broad bands formed at a wavenumber value of 3350 cm^{-1} (uncalcined) and 3315 cm^{-1} (calcined) NPs and heterostructures are due to the vibration of hydroxyl groups. This stretching vibration is associated with the surface (physisorbed) and interstitial (chemisorbed) water molecules. The short stretching vibration bands detected in the range of 2425–2260 cm^{-1} are associated with the carbonate peak due to CO_2 absorption. The nanomaterial metal bonded with oxygen (M–O) (Cu–O, Zn–O, or Ag–O) bending vibration bands, which commonly occur below 1000 cm^{-1}, are also observed in both calcined and uncalcined spectra.[52] Except for slight intensity differences, the bands detected for uncalcined ZnO NPs and c-zac are almost similar. In addition, the band detected for calcined ZnO NPs and c-zac is also almost similar. However, there is a higher wavenumber spectra shift and greater intensity for calcined NPs and heterostructures compared to the uncalcined ones. This shift is due to the increased rigidity after heat treatment, indicating the creation of stable crystalline metal oxide.[53] There is one unique bending vibration band detected at 950 cm^{-1} for the c-zac heterostructure, compared to both calcined and uncalcined ZnO NPs. This unique peak is probably associated with the Cu–O bending vibration.

2.1.6. CV investigation. The catalytic and electronic conductivity associated with the charge transfer within the electrolyte and catalyst electrode interface can be understood from the electrochemical analysis.[54] Fig. S4b† and 6 show the cyclic voltammogram-based electrochemical studies for ZnO and c-zac heterostructures, respectively. There is no reduction as well as an oxidation peak for ZnO NPs. The absence of a redox peak indicates its poor charge transfer and catalytic properties. The c-zac heterostructure has different redox peaks, which indicates the presence of charge transfer and its good catalytic properties. These redox peaks are related to the charge de-intercalation and intercalation routes.[55] The dominance of either the adsorption or diffusion charge transfer processes can be understood from the fitting of the square root of the scan rate *vs.* the peak current linear plot.[54,56] The coefficient of determination R^2 value for the c-zac heterostructure is about 0.9921 (Fig. 6 inset (I)). The well-fitting of the R^2 value for c-zac confirms the diffusion-controlled charge transfer routes. Besides, the good relationship between the diffusion-controlled transfer process theoretical value (0.5) and the slope of the

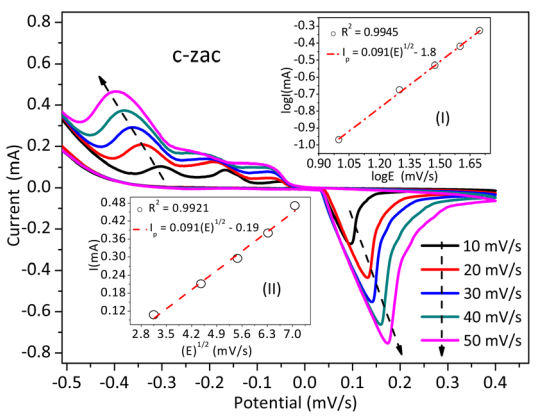

Fig. 6 C-zac electrochemical analysis using cyclic voltammetry; the inset (I) is the logarithmic relation between scan rates and the peak current linear plot; (II) is the square root of the scan rate *vs.* peak current linear plot.

logarithmic relation between the scan rates *vs.* peak current linear plot also shows the dominance of the diffusion-controlled process.[57] The slope value for c-zac for this study is 0.091, which does not confirm the dominance of a diffusion-controlled process (Fig. 6 inset (II)).

2.2. Photocatalysis activity and mechanisms

2.2.1. Photocatalytic activity. The pollutant degradation properties of synthesized ZnO NPs, Ag– and Cu–ZnO, and 15c-zac were tested on MB-D, as shown in Fig. 7, S5 and S6.† Sorption of the MB-D on the surface of the catalyst was the first step in its photocatalytic degradation.

Then, migration of the photon-induced electron and hole on the surface and reaction with adsorbed MB-D occur. The MB-D photocatalytic potential of ZnO NPs, Ag–ZnO, Cu–ZnO, and c-zac is shown in Fig. S5.† ZnO shows less potential (k = 0.0041 min^{-1}) compared to all the other heterostructures. The c-zac heterostructure has better activity (k = 0.023 min^{-1}) compared to the other heterostructures. This is due to the synergistic effects of CuO and Ag crystals. The synergistic effects here indicate a combined effect of the Cu-doped ZnO/Ag/CuO heterostructure, which enhances the optoelectrical and charge transfer properties. The catalyst dose was also optimized by taking different dosage amounts of 1, 10, 20, and 30 mg. The optimum catalyst dosage was obtained to be 20 mg (Fig. 7). The lower photocatalytic potential at lower catalyst amounts is associated with the scarcity of active sites for MB-D sorption. In addition, the lower potential at a higher dosage of 30 mg is associated with turbidity, which prevents light from reaching the surface. Besides, high catalyst amounts also result in decreasing catalyst active sites due to agglomeration in solution.[58]

To control the sorption and electrostatic interaction between the catalysts and MB-D solution, pH optimization has been conducted. Fig. 8 shows the effects of pH on the photocatalytic potential of the c-zac heterostructure. In the acidic solution (pH = 4), the catalyst is surrounded by positive hydrogen ions. The electrostatic repulsive interaction between the positively charged MB-D and the catalyst protects the dye's sorption on the catalyst's surface in acidic media. Since there is no photocatalytic reaction without sorption, less photocatalytic activity was observed in acidic pH (k = 0.020 min^{-1}). At a neutral pH of 7, the c-zac heterostructure catalyst degradation activity is relatively better than that at an acidic pH (k = 0.023 min^{-1}). As the solution pH increased to 9, the degradation potential increased significantly (k = 0.065 min^{-1}). At an alkaline pH of 9, the catalyst surface is surrounded by negatively charged hydroxyl ions. Then, the negatively charged catalyst surface and positively charged MB-D electrostatically attract each other. While comparing the photocatalysis potential of this study (k = 0.065 min^{-1}) with the related literature reports,[59,60] which have

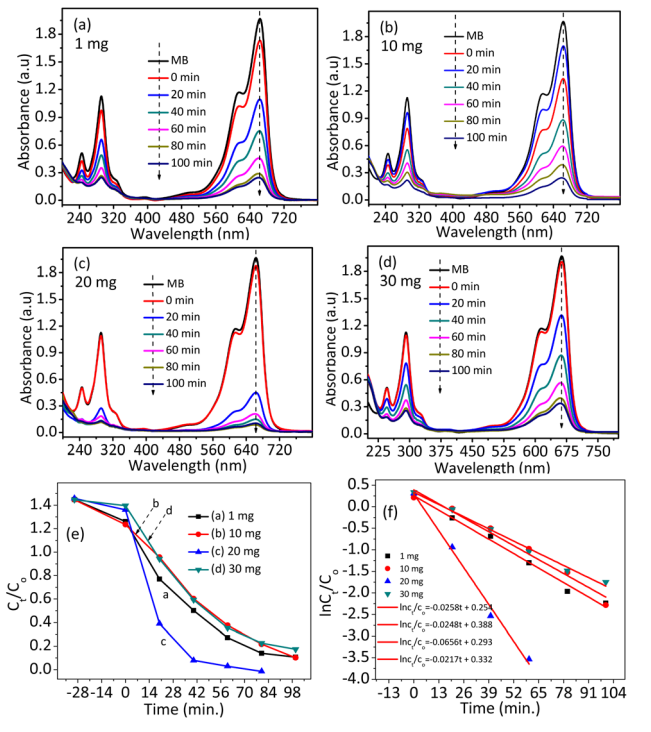

Fig. 7 Absorbance *vs.* wavelength plots of the c-zac heterostructure at an initial MB concentration of 10 ppm, an optimized solution pH of 9, and different catalyst amounts of (a) 1, (b) 10, (c) 20, (d) 30 mg, (e and f) C_t/C_0 and ln C_t/C_0 *versus* time plots of the NPs and heterostructures. A catalyst amount of 20 mg has greater photocatalytic performance. A lower catalyst amount of 1 and 10 mg lacks active sites for sorption. At a high catalyst amount of 30 mg, the catalyst protects the light from reaching the adsorbed methylene blue dye.

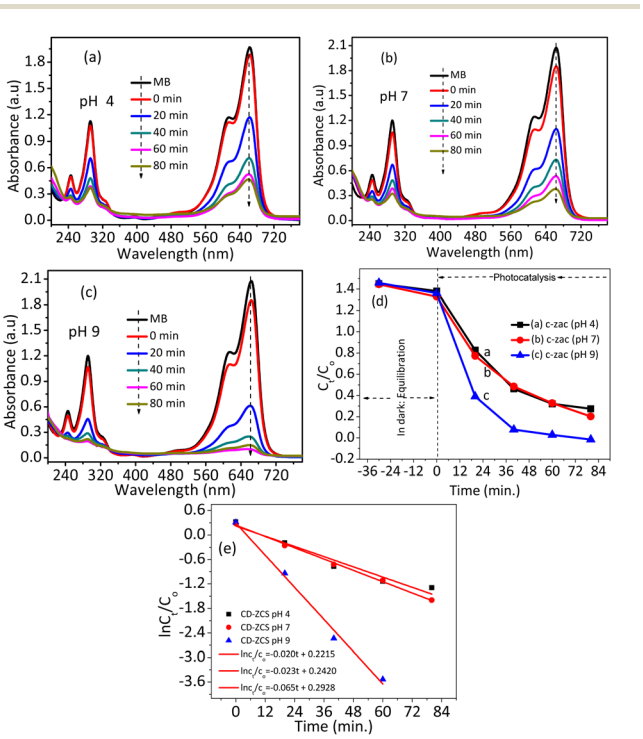

Fig. 8 The absorbance *vs.* wavelength plots of c-zac heterostructures at an initial MB concentration of 10 ppm, a catalyst amount of 20 mg, and different pH values of (a) 4, (b) 7, (c) 9, (d and e) C_t/C_0 and ln C_t/C_0 *versus* time plots of the NPs and heterostructures, respectively. The basic region (pH of 9) showed greater photocatalytic performance due to the attractive MB and catalyst electrostatic interaction effects.

a maximum rate constant value of 0.0261 min^{-1}, the photocatalytic potential for this study is much greater. This enhanced photocatalytic potential is due to the porous nature of the material, which has good pollutant adsorption ability and enhanced optoelectric and charge transfer properties.

As indicated in the XRD pattern analysis interpretation, the crystallite size for the uncalcined 15c-zac heterostructure was about 8 nm. This smaller crystallite size and greater surface area resulted in greater sorption of the dye on the catalyst surface. Of course, this greater sorption property in dark for the uncalcined 5c-zac and 15c-zac heterostructures has been conformed, as shown in Fig. S6b and S7d.† With this information, the photocatalytic activities of calcined and uncalcined ZnO NPs and the c-zac heterostructure were tested at an optimized pH of 9. However, the test showed that the photocatalytic potential for calcined ZnO NPs ($k = 0.028$ min^{-1}) and c-zac heterostructure ($k = 0.067$ min^{-1}) is much greater than that of uncalcined ZnO NPs ($k = 0.015$ min^{-1}) and c-zac heterostructure ($k = 0.012$ min^{-1}). The decrease in photocatalysis potential for the uncalcined materials is due to a lack of crystallinity and the blockage of the nanocrystals from light by the uncalcinated impurities. Besides, to see the effects of dopant amount, the calcined 5c-zac heterostructure was also tested. Here, the 5c-zac heterostructure showed lower activity ($k = 0.017$ min^{-1}) than the 15c-zac heterostructure, as shown in Fig. S6g.† The greater photocatalytic potential of heterostructures is a result of the improvement in optical properties and the presence of charge transfer through the interface. The charge transfer is associated with the electron getting relaxation time without recombination.

2.2.2. Mechanism. The enhanced photocatalytic potential mechanism of the 15c-zac heterostructure was proposed (Fig. S7†). The Motte–Schottky plot and DRS-UV-vis analysis were used to determine the band edge potential. The ZnO CB and VB edge potentials are obtained to be −0.87 V and 2.32 eV, respectively. While the CuO CB and VB edge potentials are −0.92 and −0.49 eV, respectively.[44] During contact, first the Fermi level redistribution until equilibration occurs as a result of differences in the work function. Then, the development of an internal electric field, or accumulated layer, between the two semiconductor interfaces as well as band edge bending occurred.[61,62] Presently, charge transfer mechanisms such as type II (staggered), Z-, and S-schemes are proposed (Fig. S7a–c†). In the type II mechanism, electrons migrate from the CuO CB to the ZnO CB. The holes migrate from ZnO VB to CuO VB. However, the VB potential of CuO (−0.49 eV) is more negative than the standard reduction potential of $^{\bullet}OH/H_2O$ (−2.38 eV). Thus, water cannot be oxidized by the accumulated holes in the VB.[12] In the Z-scheme mechanism, the weaker thermodynamic potential electrons on the ZnO CB recombine with CuO VB (Fig. S7b†). Thus, the CuO CB electrons and ZnO VB holes exist with greater reduction and oxidation potential, respectively. Besides, in the S-scheme mechanism (Fig. S7c†), the internal electric field assists in the electrostatic attraction of electrons and holes. Thus, the electrons from ZnO CB and holes from CuO VB come together and result in quenching at the interface.[63] Here also, the CuO CB electrons and ZnO VB holes are present with greater energy.

Thus, reduction and oxidation of oxygen and water for the generation of electroactive species ($^{\bullet}O_2^-$ and $^{\bullet}OH$) occur, respectively. In both Z- and S-scheme mechanisms, electrons and holes with less thermodynamic energy are lost. Recently, incorporating a charge mediator such as silver between the two semiconductors was proposed (Fig. S7d†). This mediator insertion was proposed to resolve the electron–hole recombination and quenching problems in the Z- and S-scheme mechanisms.[13,14] Copper oxide is a photocatalyst that has enhanced visible light absorption properties.[64] Silver also has a surface plasmon resonance property, which involves the oscillation of electrons with the electric field.[14] Thus, forming silver and CuO heterojunction can enhance the visible light absorption properties of ZnO and also extend the charge relaxation time for the generation of reactive oxygen species. In this study, the photocatalytic activities of 15c-zac are much better than those of Cu-doped ZnO/CuO as well as Ag/ZnO heterostructures. This indicates that the Z- or S-scheme mechanism in the presence of a silver mediator is the most likely mechanism.

2.2.3. Reusability test. Fig. 9 shows the stability and photocatalytic reusability performance tests for the 15c-zac heterostructure. The photocatalytic performance of 15c-zac for the first three cycles is good (Fig. 9a). The obtained rate constant for the 1st (0.0656 min^{-1}), 2nd (0.0641 min^{-1}), and 3rd (0.0620 min^{-1}) cycles shows the presence of slight performance-decreasing behaviour (Fig. 9b). However, the 4th cycle shows a greater rate constant reduction (0.0469 min^{-1}) compared to the others. This performance reduction for the 4th cycle is probably associated with the loss in material crystallinity. Fig. 9c shows the XRD pattern analysis results of the 15c-zac heterostructure before the experiment and after the 4th cycle reusability test. The material's crystallinity has a crucial effect on its catalytic applications; the higher the crystallinity, the greater its catalytic potential.[65] The XRD pattern analysis shows that the crystallinity of the material before the photocatalysis test is better than after the test, which explains why the potential after the 4th cycle decreased.

3. Experimental

3.1. Chemicals

The polyvinyl alcohol polymer (PVA), zinc nitrate ($Zn(NO_3)_2{\cdot}6H_2O$), copper nitrate ($Cu(NO_3)_2$), and silver nitrate ($AgNO_3$, 99%) are chemicals used for this work. These common chemicals are used immediately after purchase without further laboratory purification.

3.2. Synthesis of NPs and heterostructures

HSAB theory is a significant theory for selecting dopant–host reactivity balance. Here, solvent hardness is also another crucial consideration for dopant–host reactivity. The soft acid dopant can diffuse and be incorporated into the borderline or hard host acid in hard solvents like alcohol and water.[66,67] There are about

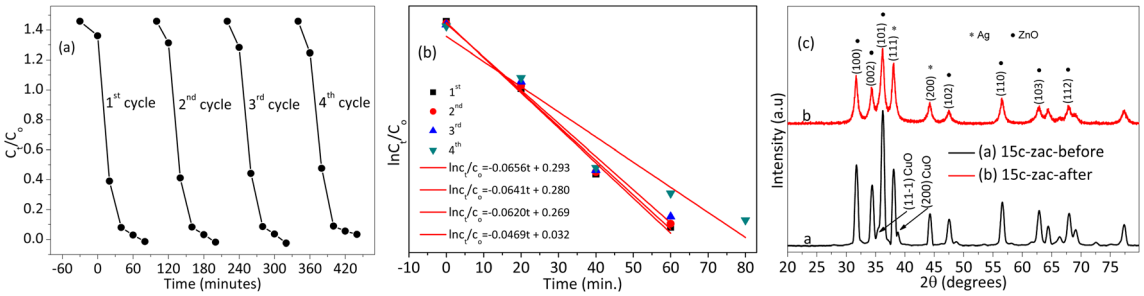

Fig. 9 Reusability and XRD pattern test for optimized 15c-zac heterostructure: (a and b) four-cycle C_t/C_0 *versus* time and ln C_t/C_0 *versus* time photocatalytic performance reusability test, respectively, (c) the XRD pattern plots of 15c-zac heterostructure before and after the photocatalysis experiment.

five common procedures used for the diffusion of dopants in the host lattice.[66] The single-source precursors using nitrate metal salts were used for this study. Specifically, the copper and silver soft acid dopants were used to diffuse and exchange Zn in the ZnO lattice.

In detail, to synthesize ZnO NPs, first, 1.00 g of PVA was completely dissolved in 50 mL of distilled water while stirring on a magnetic stirrer at a temperature of 70–80 °C.[24,29] The PVA aqueous solution was cooled down to a temperature of 50 °C. Then, the $Zn(NO_3)_2.6H_2O$ salt precursor was added and dissolved for about 30 minutes. The solution was then constantly heated to 100 °C (4 h) to remove the solvent and convert the sol to gel. The gel was further heated and combusted by gently increasing the temperature in the range of 150–250 °C. Lastly, the spongy, high-volume combusted product was crushed and calcined at 450 °C for 1 hour. Besides, the effects of PVA amount (0.10–2.00 g), synthesis temperature (30–90 °C), calcination time (1/2–3 h), and dopant amount (0.5–20%) were studied and optimized. To synthesize the c-zc, za, and c-zac heterostructures, the same above-mentioned steps are followed, except for adding the copper nitrate and silver nitrate salt precursors.

3.3. Photocatalytic activity

The photocatalytic activity was conducted by focusing the xenon lamp at a distance of 2 cm. A constant 10 ppm initial concentration of MB-D was used during the experiment. The degradation potential of ZnO NPs, za, c-zc, and c-zac were first tested and optimized. The catalyst amount (1, 10, 20, and 30 mg) and solution pH (4, 7, and 9) were optimized. The degradation potential of calcined and uncalcined ZnO NPs and c-zac with two different dopant concentrations was also tested. To attain catalyst-dye adsorption/desorption equilibration, first the mixture was continuously stirred in the dark for 30 minutes. After the equilibration time, the catalyst-dye mixture was irradiated with a broad-spectrum xenon lamp. An electric fan and water circulation were used to control the reactor temperature. The dye degradation potential was controlled using the UV-vis spectrophotometer with a twenty-minute interval. The percentage efficiency and reaction dynamics were calculated based on the percentage and pseudo-first-order kinetic equations, respectively.[36]

3.4. Characterizations

Thermal stability is determined by a thermogravimetric-differential thermal analyzer (DTG-60H). Crystallinity and average crystallite size are examined by X-ray diffractometer (Shimadzu-7000). Morphology, composition, and elemental mapping are studied by field emission-scanning electron microscopes (ZEISS SIGMA VP). Optical properties are observed by double-beam ultraviolet-visible spectroscopy (P9 spectrophotometer). The cyclic voltammetry (CV) (a CHI608E workstation; potentiostat, scan rate, 0.03 (V s^{-1}), sensitivity (0.001 A V^{-1})) electrochemical analyzer was used to examine the electrochemical properties of ZnO and c-zac. Here, the respective 70 : 15 : 15 ratios of graphite powder, silicon oil, and catalyst were mixed to create the NPs and heterostructure paste. Thus, the catalyst paste-modified electrodes as working, the Ag/AgCl standard electrode as a reference, and the platinum wire as a counter electrode were used in the three-electrode system. Besides, a 0.1 M Na_2SO_4 aqueous solution was used for the Mott–Schottky analysis at four different frequencies of 1, 10, 100, and 1000 Hz with amplitude of 10 mV.

4. Conclusions

Here, a porous Cu-doped ZnO/Ag/CuO heterostructure is effectively synthesized by the bottom-up combustion approach. A 1.00 g of PVA polymer was obtained to be the optima. Besides, the synthesis temperature of 50 °C and the calcination time of 1 hour were optimized and fixed. The Cu-doped ZnO and ZnO/Ag/CuO formations were confirmed from the HRTEM image and XRD pattern analysis. The obtained crystallite size (XRD) was found to be 10–25 nm. The particle size (TEM) was found to be within the range of 40–75 nm. The porosity observed on the FESEM image is associated with gaseous by-product evolution. The solubility of copper dopant was found to be much better than that of silver. The good silver metal surface distribution was confirmed by the elemental mapping FESEM-EDS analysis. The optical property change for ZnO is associated with copper 3d mid-gap state formation and heterojunction. The mid-gap level is a result of host–dopant sp–d strong exchange interaction. The c-zac heterostructure (k = 0.067 min^{-1}) showed enhanced methylene blue degradation potential compared to single ZnO (k = 0.0041 min^{-1}). The photocatalytic reusability

test is also tested and found to be effective until the third cycle. This greater potential is due to the enhanced optoelectric and charge transfer properties. The Z- or S-scheme in the presence of silver as a mediator is a possible mechanism related to the application. However, the dopant level distribution (copper case) using STEM microscopy is our future work. Thus, this modified heterostructure that has good photocatalytic dye degradation potential has noble future outlooks as an environmental pollution control application.

Data availability

The data supporting this article have been included as part of the ESI.†

Author contributions

Abbay Gebretsadik: investigation and writing—original draft; Bontu Kefale: investigation; Chaluma Sori: data curation; Dereje Tsegaye: writing—review & editing, project administration, and supervision; H. C. Ananda Murthy: validation and writing—review & editing; Buzuayehu Abebe: conceptualization, data curation, methodology, and supervision.

Conflicts of interest

There are no conflicts to declare.

Acknowledgements

The authors acknowledge Adama Science and Technology University for financial support (ASTU/AS-R/052/2022).

Notes and references

1 P. O. Oladoye, T. O. Ajiboye, E. O. Omotola and O. J. Oyewola, *Results Eng.*, 2022, **16**, 100678.
2 B. Abebe, N. K. Gupta and D. Tsegaye, *RSC Adv.*, 2024, **14**, 17338–17349.
3 F. Hu, D. Yu, M. Ye, H. Wang, Y. Hao, L. Wang, L. Li, X. Han and S. Peng, *Adv. Energy Mater.*, 2022, **12**, 1–10.
4 X. Sun, L. Li, S. Jin, W. Shao, H. Wang, X. Zhang and Y. Xie, *eScience*, 2023, **3**, 100095.
5 Y. Hao, F. Hu, S. Zhu, Y. Sun, H. Wang, L. Wang, Y. Wang, J. Xue, Y. Liao, M. Shao and S. Peng, *Angew. Chem., Int. Ed.*, 2023, **62**, 1–8.
6 R. Ebrahimi, K. Hossienzadeh, A. Maleki, R. Ghanbari, R. Rezaee, M. Safari, B. Shahmoradi, H. Daraei, A. Jafari, K. Yetilmezsoy and S. H. Puttaiah, *J. Environ. Health Sci. Eng.*, 2019, **17**, 479–492.
7 A. Iribarren, E. Hernández-Rodríguez and L. Maqueira, *Mater. Res. Bull.*, 2014, **60**, 376–381.
8 J. H. Zheng, J. L. Song, Q. Jiang and J. S. Lian, *J. Mater. Sci.: Mater. Electron.*, 2012, **23**, 1521–1526.
9 B. Divband, M. Khatamian, G. R. K. Eslamian and M. Darbandi, *Appl. Surf. Sci.*, 2013, **284**, 80–86.
10 T. N. Q. Trang, T. B. Phan, N. D. Nam and V. T. H. Thu, *ACS Appl. Mater. Interfaces*, 2020, **12**, 12195–12206.
11 S. Wang, F. Jia, X. Wang, L. Hu, Y. Sun, G. Yin, T. Zhou, Z. Feng, P. Kumar and B. Liu, *ACS Omega*, 2020, **5**, 5209–5218.
12 J. Ran, M. Jaroniec and S. Qiao, *Adv. Mater.*, 2018, **30**, 1–31.
13 K. Xu, Z. Liu, S. Qi, Z. Yin, S. Deng, M. Zhang and Z. Sun, *RSC Adv.*, 2020, **10**, 34702–34711.
14 S. A. Mahyoub, A. Hezam, F. A. Qaraah, K. Namratha, M. B. Nayan, Q. A. Drmosh, D. Ponnamma and K. Byrappa, *ACS Appl. Energy Mater.*, 2021, **4**, 3544–3554.
15 X. Liu, A. Dang, T. Li, Y. Sun, T.-C. Lee, W. Deng, S. Wu, A. Zada, T. Zhao and H. Li, *ACS Sens.*, 2023, **8**, 1287–1298.
16 A. H. Rakhsha, H. Abdizadeh, E. Pourshaban, M. R. Golobostanfard, V. R. Mastelaro and M. Montazerian, *Materialia*, 2019, **5**, 100212.
17 A. Modwi, K. K. Taha, L. Khezami, M. Boudina, M. Khairy, O. K. Al-Duaij and S. Talab, *Z. Phys. Chem.*, 2021, **235**, 745–767.
18 K. Xu, J. Wu, C. F. Tan, G. W. Ho, A. Wei and M. Hong, *Nanoscale*, 2017, **9**, 11574–11583.
19 R. Kant, R. Jakhar and A. Sharma, *Mater. Technol.*, 2022, **37**, 2679–2691.
20 E. Novitskaya, J. P. Kelly, S. Bhaduri and O. A. Graeve, *Int. Mater. Rev.*, 2021, **66**, 188–214.
21 S. L. González-Cortés and F. E. Imbert, *Appl. Catal., A*, 2013, **452**, 117–131.
22 B. Cai, H. Liu and W. Han, *Catalysts*, 2020, **10**, 1027.
23 H. H. Nersisyan, J. H. Lee, J.-R. Ding, K.-S. Kim, K. V. Manukyan and A. S. Mukasyan, *Prog. Energy Combust. Sci.*, 2017, **63**, 79–118.
24 Y. Gao, F. Meng, X. Li, J. Z. Wen and Z. Li, *Catal. Sci. Technol.*, 2016, **6**, 7800–7811.
25 F. Deganello and A. K. Tyagi, *Prog. Cryst. Growth Charact. Mater.*, 2018, **64**, 23–61.
26 D.-M. Liu, T. Troczynski and W. J. Tseng, *Biomaterials*, 2002, **23**, 1227–1236.
27 J. Wang and L. L. Shaw, *J. Mater. Sci.: Mater. Med.*, 2009, **20**, 1223–1227.
28 V. K. LaMer and R. H. Dinegar, *J. Am. Chem. Soc.*, 1950, **72**, 4847–4854.
29 B. Liu, Y. You, H. Zhang, H. Wu, J. Jin and H. Liu, *RSC Adv.*, 2016, **6**, 110349–110355.
30 P. Budrugeac, *J. Therm. Anal. Calorim.*, 2008, **92**, 291–296.
31 H. Yang, S. Xu, L. Jiang and Y. Dan, *J. Macromol. Sci., Part B: Phys.*, 2012, **51**, 464–480.
32 J. Selvi, S. Mahalakshmi, V. Parthasarathy, C. Hu, Y. Lin, K. Tung, R. Anbarasan and A. A. Annie, *Polym. Compos.*, 2019, **40**, 3737–3748.
33 S. A. Ansari, M. M. Khan, M. O. Ansari, J. Lee and M. H. Cho, *J. Phys. Chem. C*, 2013, **117**, 27023–27030.
34 F. A. Alharthi, A. A. Alghamdi, N. Al-Zaqri, H. S. Alanazi, A. A. Alsyahi, A. El Marghany and N. Ahmad, *Sci. Rep.*, 2020, **10**, 20229.
35 J. Liu, J. Li, F. Wei, X. Zhao, Y. Su and X. Han, *ACS Sustain. Chem. Eng.*, 2019, **7**, 11258–11266.

36 B. Abebe, E. A. Zereffa and H. C. A. Murthy, *ACS Omega*, 2021, **6**, 954–964.
37 K. Schneider, *J. Mater. Sci.: Mater. Electron.*, 2020, **31**, 10478–10488.
38 S. Boulahlib, K. Dib, M. Özacar and Y. Bessekhouad, *Opt. Mater.*, 2021, **113**, 110889.
39 H. Cai, P. Liang, Z. Hu, L. Shi, X. Yang, J. Sun, N. Xu and J. Wu, *Nanoscale Res. Lett.*, 2016, **11**, 104.
40 Y. Ma, T.-W. Choi, S. H. Cheung, Y. Cheng, X. Xu, Y.-M. Xie, H.-W. Li, M. Li, H. Luo, W. Zhang, S. K. So, S. Chen and S.-W. Tsang, *Nanoscale*, 2019, **11**, 8736–8743.
41 B. D. Yuhas, D. O. Zitoun, P. J. Pauzauskie, R. He and P. Yang, *Angew. Chem., Int. Ed.*, 2006, **45**, 420–423.
42 N. Ali, V. A. Ramasamy, Z. A. Khan, K. Tarafder, A. Kumar, M. K. Wadhwa, B. Singh and S. Ghosh, *Sci. Rep.*, 2019, **9**, 20039.
43 S. Phanichphant, A. Nakaruk, K. Chansaenpak and D. Channei, *Sci. Rep.*, 2019, **9**, 16091.
44 S. Ruan, W. Huang, M. Zhao, H. Song and Z. Gao, *Mater. Sci. Semicond. Process.*, 2020, **107**, 104835.
45 B. Subash, B. Krishnakumar, R. Velmurugan, M. Swaminathan and M. Shanthi, *Catal. Sci. Technol.*, 2012, **2**, 2319.
46 H. A. Thabit, N. A. Kabir, A. K. Ismail, S. Alraddadi, A. Bafaqeer and M. A. Saleh, *Nanomaterials*, 2022, **12**, 3068.
47 M. Pashchanka, R. C. Hoffmann, A. Gurlo, J. C. Swarbrick, J. Khanderi, J. Engstler, A. Issanin and J. J. Schneider, *Dalton Trans.*, 2011, **40**, 4307.
48 R. S. Zeferino, M. B. Flores and U. Pal, *J. Appl. Phys.*, 2011, **109**, 014308.
49 E. Carlos, R. Martins, E. Fortunato and R. Branquinho, *Chem.–Eur. J.*, 2020, **26**, 9099–9125.
50 P. Rong, Y.-F. Jiang, Q. Wang, M. Gu, X.-L. Jiang and Q. Yu, *J. Mater. Chem. A*, 2022, **10**, 6231–6241.
51 B. Abebe and H. C. A. Murthy, *RSC Adv.*, 2022, **12**, 5816–5833.
52 M. L. da Silva-Neto, M. C. A. de Oliveira, C. T. Dominguez, R. E. M. Lins, N. Rakov, C. B. de Araújo, L. de S. Menezes, H. P. de Oliveira and A. S. L. Gomes, *Sci. Rep.*, 2019, **9**, 11765.
53 L. Lan, G. Gnappi and A. Montenero, *J. Mater. Sci.*, 1993, **28**, 2119–2123.
54 C.-F. Tang, S. A. Kumar and S.-M. Chen, *Anal. Biochem.*, 2008, **380**, 174–183.
55 J. Liu, T. Xu, X. Sun, J. Bai and C. Li, *J. Alloys Compd.*, 2019, **807**, 151652.
56 R. Suresh, K. Giribabu, R. Manigandan, A. Stephen and V. Narayanan, *RSC Adv.*, 2014, **4**, 17146.
57 D. Thomas, Z. Rasheed, J. S. Jagan and K. G. Kumar, *J. Food Sci. Technol.*, 2015, **52**, 6719–6726.
58 Z. Mirzaeifard, Z. Shariatinia, M. Jourshabani and S. M. R. Darvishi, *Ind. Eng. Chem. Res.*, 2020, **59**, 15894–15911.
59 M. Rabbani, J. Shokraiyan, R. Rahimi and R. Amrollahi, *Water Sci. Technol.*, 2021, **84**, 1813–1825.
60 M. Xu, Y. Chen, W. Y. Hu, Y. T. Liu, Q. P. Zhang, H. Yuan, X. Y. Wang, J. X. Zhang, K. Y. Luo, J. Li and G. Xiong, *J. Phys. D Appl. Phys.*, 2020, **53**, 025106.
61 G. Sun, J. Zhang, B. Cheng, H. Yu, J. Yu and J. Xu, *Chem. Eng. J.*, 2023, **476**, 146818.
62 G. Sun, Z. Tai, F. Li, Q. Ye, T. Wang, Z. Fang, L. Jia, W. Liu and H. Wang, *Small*, 2023, **19**, 19251–19257.
63 Z. Jiang, B. Cheng, Y. Zhang, S. Wageh, A. A. Al-Ghamdi, J. Yu and L. Wang, *J. Mater. Sci. Technol.*, 2022, **124**, 193–201.
64 P. Raizada, A. Sudhaik, S. Patial, V. Hasija, A. A. P. Khan, P. Singh, S. Gautam, M. Kaur and V.-H. Nguyen, *Arabian J. Chem.*, 2020, **13**, 8424–8457.
65 S. Kuriakose, B. Satpati and S. Mohapatra, *Phys. Chem. Chem. Phys.*, 2014, **16**, 12741–12749.
66 R. Buonsanti and D. J. Milliron, *Chem. Mater.*, 2013, **25**, 1305–1317.
67 H. Hu, H. He, J. Zhang, X. Hou and P. Wu, *Nanoscale*, 2018, **10**, 5035–5046.